Coupled Fluid/Solid Numerical Investigation of the Heat Load on a Lobed Scramjet Strut Injector

P. Gerlinger,[1] Y.-H. Simsont [2]

Abstract

The thermal load on a lobed scramjet (supersonic combustion ramjet) strut injector is investigated numerically for Mach 8 flight conditions. For this purpose, coupled 3D RANS (Reynolds Averaged Navier-Stokes) simulations of the supersonic external flow field around the strut injector and the subsonic strut internal hydrogen flow are performed. The temperature distribution in the solid strut material is simulated by a separate code, which exchanges data with the solver for the external and internal flow fields. Due to the predominantly low Mach numbers inside the strut, an all-Mach number preconditioning is required to enable convergence of the compressible flow solver. The air flow Mach number in the combustion chamber is 3. Different strut materials (copper, silicone carbide, molybdenum, and tungsten) with different heat capacities and thermal conductivities are compared. Moreover, the impact of the height of the blunt tip of the strut on the heat load is investigated. Due to a small detached normal shock wave upstream of the strut, the thermal load at the tip is very high. Unfortunately this part is difficult to cool. In order to keep the strut temperature acceptable, it is cooled actively by the hydrogen, which is injected later for combustion. A sophisticated internal strut structure is used to direct the hydrogen towards regions of highest heat load. Different strut geometries, fuel mass fluxes (stoichiometric ratios), and strut materials are investigated.

Keywords: *Scramjet, strut injector, conjugate heat transfer, strut cooling.*

1. Introduction

The cooling of scramjet engines is an important issue for practical applications. Due to the high total temperatures of hypersonic flows, this is a complicated task. Usually the most extreme heat loads in a scramjet appear in the combustion chamber. Here the incoming air is compressed already to enable combustion and the flow velocity is relatively low. Moreover, there is heat release due to combustion. Similar as in rocket combustion chambers, the injected fuel is the best choice to be used for cooling. Otherwise an additional cooling fluid is needed with corresponding tanks and supply systems, increasing the weight. Thus the question arises, if there is enough fuel to cool all relevant parts (combustor walls, fuel injectors, and fractions of inlet and nozzle) at continuous operation. In case of flame stabilization by cavities or in case of sub- or supersonic combustion close to solid walls, the nearby material is exposed to even higher temperatures. Regenerative, film, and transpiration cooling techniques are under investigation [1-4]. Additionally, cryogenic fuels such as liquid hydrogen or methane can be chosen, which, similar to rocket engines, offer good cooling properties before they are burned. Another possibility are hydrocarbon fuels (e.g. octane, dodecane), which due to endothermic chemical cracking (e.g. in the cooling channels), can work as a heat sink [5] under certain conditions. A second advantage of this procedure is, that after cracking the products often have shorter ignition delay times (e.g. due the production of hydrogen). Nevertheless, the cooling capability of the fuel is limited especially at higher flight Mach numbers.

[1]*University of Stuttgart, Institute of Combustion Technology of Aerospace Engineering, Pfaffenwaldring 38-40, Germany, email: peter.gerlinger@dlr.de*
[2]*University of Stuttgart, Institute of Combustion Technology of Aerospace Engineering, Pfaffenwaldring 38-40, Germany*
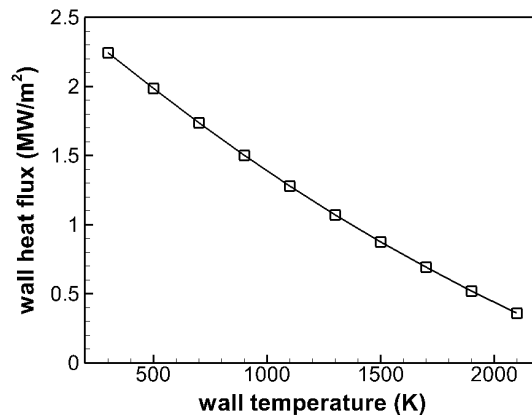
Fig 1. Calculated wall heat fluxes of a Mach 3 turbulent boundary layer (Mach 8 flight conditions) using different constant wall temperatures.

A possible concept for a fuel supply of scramjet engines is the use of strut injectors, located at the channel axis [6-12]. In this way the fuel is directly injected into the core of the air stream and it is possible to achieve a fast and efficient mixing [12]. Moreover, under ideal conditions, the flame is positioned downstream of the strut and neither causes an additional heat load for the strut nor for the walls [9,12,13]. The following simulations are based on this assumption. This allows conjugate heat transfer strut injector studies without taking combustion into account. In order to achieve a good mixing, a lobed strut structure is used, which has proven to enable a rapid mixing due to creation of streamwise vorticity [12]. A disadvantage of struts compared to wall injectors is the cooling challenge, which is the topic of this paper. Located at the center of the channel the strut is exposed to the incoming high speed flow. In the investigated test case with Mach 8 flight conditions, the static temperature inside the combustor is approximately 1160 K, which corresponds to a total temperature of about 3250 K. Thus, especially the tip of the strut may suffer from very high temperatures. Moreover, fuel is required for an active cooling which may never be switched off completely. The required minimum fuel mass flow is an important parameter for a given set of operating conditions.

To approximate the wall heat fluxes at the Mach 8 flight and Mach 3 combustor entrance conditions studied in this paper (see Table 1), flat plate boundary layers with different constant wall temperatures are calculated. The wall heat fluxes of these fully turbulent air boundary layers (after 1 m plate length) strongly depend on the chosen wall temperature, as can be seen in Fig. 1. If the wall temperature could be increased from 700 K to 1900 K, the wall heat flux would decrease by 70%. Thus less coolant is required if the combustor walls are able to sustain higher temperatures. This could be an advantage if ceramic composite materials are used. On the other hand the material should have a good conductivity and emissivity, too.

In the literature there are a number of papers, where cooling concepts of complete scramjet engines are investigated in simplified ways [1,14-16]. However, up to now only few studies exist, which investigate cooling concepts for parts of a scramjet combustor (e.g. wall structures, cooling channels [17], or injectors [6,7,10]) by detailed 3D numerical simulations. This paper treats such conjugate heat transfer simulations. The investigated strut geometry was first presented in [18] and a geometrical variant of it has been tested [19]. A first simulation with heat transfer followed [6,7] for real flight conditions but one equivalence ratio ($\Phi = 0.7$), only. Later experimental and numerical studies of a similar strut have been performed at laboratory conditions with a total temperature of 1300 K [10]. The present paper studies (again for Mach 8 flight conditions with a total temperature of 3250 K)

- the impact of the geometrical choice of the tip of the strut on its thermal load;

- the influence of different hydrogen mass fluxes on cooling;

- the effect of different strut materials on heat fluxes and peak temperatures.

To this end a large number of simulations were performed which give insight into the fluid dynamical processes as well as in the temperature distributions in the strut injectors. Due to the large variety of possible strut materials and thus material properties, this paper does not have the purpose to recommend a certain material for a strut. Instead we want to show the impact of a given thermal conductivity and specific heat of a material on the heat flux rates, maximum temperature in the strut, and the required mass flux of coolant.

2. Numerical solvers

To simulate the gas phase flows inside and outside the strut, the averaged set of extended three-dimensional transport equations (continuity, momentum, energy, species, and turbulence) is solved with the in-house code TASCOM3D [20-22]. TASCOM3D has been developed for high speed flows with and without combustion over more than two decades. It uses an implicit Lower-Upper Symmetric Gauß-Seidel (LU-SGS) algorithm [23,24] for time integration. For turbulence closure, a low-Reynolds-number q-ω turbulence model [25] is employed in the present study. It is based on the turbulence variables $q = \sqrt{k}$ and $\omega = \epsilon/k$, which are connected to the turbulent kinetic energy k and its dissipation rate ϵ. The accuracy of TASCOM3D is up to sixth order in space and 3rd order in time [22]. However, the steady-state simulations presented in this paper are calculated with a second order discretization. In contrast to time accurate unsteady flows, this has proven to be sufficient for steady-state RANS simulations [22]. For the interface flux calculation, the AUSM$^+$-up flux vector splitting [26] is used. This method works well even at very low Mach numbers. In the present case, there is a large disparity in flow Mach number between the internal low speed flow which dominates large parts inside the strut and the acceleration in the nozzle up to the (external) combustor Mach number of 3. An all-Mach number preconditioning [27,7] was required to achieve convergence of the compressible flow solver. The calculation of the viscous fluxes is realized by a second order central discretization. Both inviscid and viscous fluxes are included in the Jacobian matrices of the implicit solver and enable a high numerical stability. This is necessary for the following simulations, which are not only distinguished by large differences in Mach number but also by very fine high aspect ratio grids close to solid walls, shock waves, and a complex flow field. A three component gas mixture (nitrogen, oxygen, hydrogen) is considered in the present investigations. TASCOM3D is fully vectorized and parallelized using MPI and is based on structured multi-block grids. Both the turbulent Prandtl and Schmidt numbers are assumed to be 0.7. The code has been validated over many years, especially for high speed flows and supersonic combustion, using a large number of test cases. Some examples may be found in [6,12,13,18-22]. Moreover, validations have been performed for an identical strut at lower temperatures and Mach numbers which could be realized in a ground test facility [12,18,19].

To calculate the temperature distribution inside the strut the three-dimensional energy equation in a temperature formulation

$$\rho V c_p \frac{\partial T}{\partial t} + \oint_S \lambda \nabla T dS = 0 \qquad (1)$$

is solved, where the heat fluxes are calculated from Fourier's law. The properties of the strut material are the constant density ρ, the temperature dependent specific heat $c_p(T)$, and the thermal conductivity $\lambda(T)$. V is the volume and S the surface of a computational cell. At the interface between gas and solid a constant heat flux is assumed and the wall temperature is calculated from

$$\lambda_g \frac{T_g - T_{wall}}{\Delta y_g} = \lambda_s \frac{T_{wall} - T_s}{\Delta y_s} \,, \qquad (2)$$

where g indicates the gaseous and s the solid phase. A cell centered finite-volume discretization is used both for the gas phase and the solid. Thus T_g and T_s are cell center temperatures of the first fluid and solid volume, and Δy_g and Δy_s are the corresponding distances to the wall, respectively. This approach requires a good spatial resolution of the viscous sublayer and thus very fine grids close to solid walls. Moreover, λ_g, T_g, and Δy_g have to be transferred from the gas to the solid phase solver. Because the
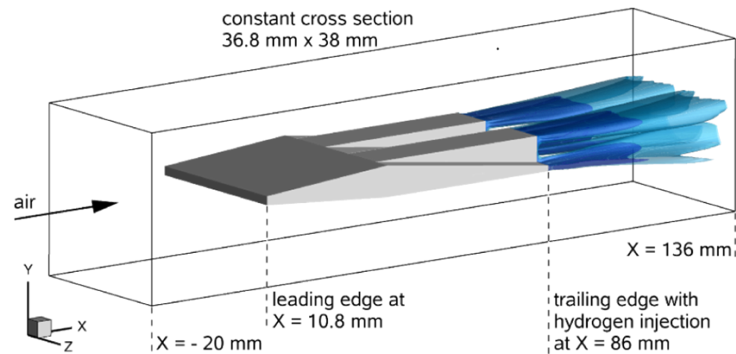
Fig 2. Simulated channel segment with lobed strut injector and two iso-surfaces (in blue) of constant hydrogen mass fractions.

computational grids are not identical at the gas/solid interfaces, these values are interpolated between both grids to the positions, where they are required. In the opposite direction T_w is returned to the gas phase solver and again, has to be interpolated to the correct gas phase position. This data exchange is performed in the same way from the external and the internal flows towards the solid strut. Due to the chosen central discretization, a septa-diagonal set of equations has to be solved for the solid in 3D. This is done with the in-house code HeatEQ [7], which is based on the Douglas-Gunn Alternating Direction Implicit (ADI) method [28]. This three-step algorithm is unconditionally stable and second order accurate in space and time. The resulting tri-diagonal sets of equations are solved efficiently by a Thomas algorithm [29]. HeatEQ uses structured multi-block grids, it is vectorized and parallelized and has been validated against analytical solutions and experimental test cases.

3. Test case and numerical set up

3.1. Strut and channel geometry

The simulated channel part with lobed strut injector is shown in Fig. 2. The channel has a constant cross section with a height of 38 mm and 36.8 mm depth. In previous investigations [18] the strut injector had a sharp tip, as can be seen in the upper left sketch of Fig. 3. The origin of the channel coordinate system is at the front end of the sharp tip strut on the channel axis. In this paper two blunt front geometries for the strut are investigated (lower two pictures on the left side of Fig. 3), which differ in the wall thickness of the vertical front part (2.4 mm and 0.9 mm). A reduction of the wall thickness enables a better cooling. Due to the tip cutting the length of the original strut (86 mm) reduces to 75.2 mm and 73.7 mm and the front end positions are at $x = 10.8$ mm and 12.3 mm, respectively. All simulations start at $x = -20$ mm to cover possible upstream effects. In case of the blunt front injector of Fig. 2 (with 2.4 mm front wall thickness), the inflow is 30.8 mm upstream of the injector. The strut is mounted at the channel side walls allowing heat transfer from the strut towards the walls. All struts end at $x = 86$ mm, where hydrogen is injected but the simulated flow fields still extend 50 mm downstream of the struts up to the $x = 136$ mm position. Non-reactive flows are simulated, but even in case of combustion [12] the flame usually is lifted and does not increase the thermal load on the strut. Moreover, an upstream movement of the flame along the outer strut surface has to be avoided because it can induce thermal choking.

Figure 3 (right side) shows a sketch of the lobed strut injector investigated. Hydrogen is injected through a nozzle at the blunt end of the strut (at supersonic speed) in the combustion chamber. As explained before, first investigations (also in experiment) used a sharp tip for the strut [18,12,10]. At real flight conditions however, such a tip would burn down because it can not be cooled efficiently. At laboratory conditions with total temperatures between 1300 K and 1400 K a copper strut with sharp tip worked well even at continuous operation [10]. The maximum temperatures observed at the tip are around 900 K. However, at Mach 8 flight conditions, only few materials would be able to withstand the much more
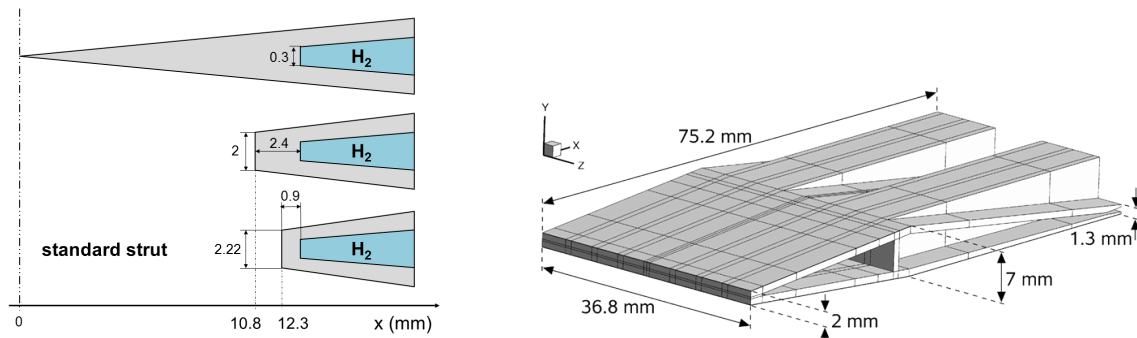
Fig 3. Investigated tips for the lobed strut injector (left side), sizes in mm. Geometry (right side) of the strut with 2.4 mm thickness of the blunt front (corresponds to the middle picture left side), block structure, and lengths. Sketches on the left side are not to size.
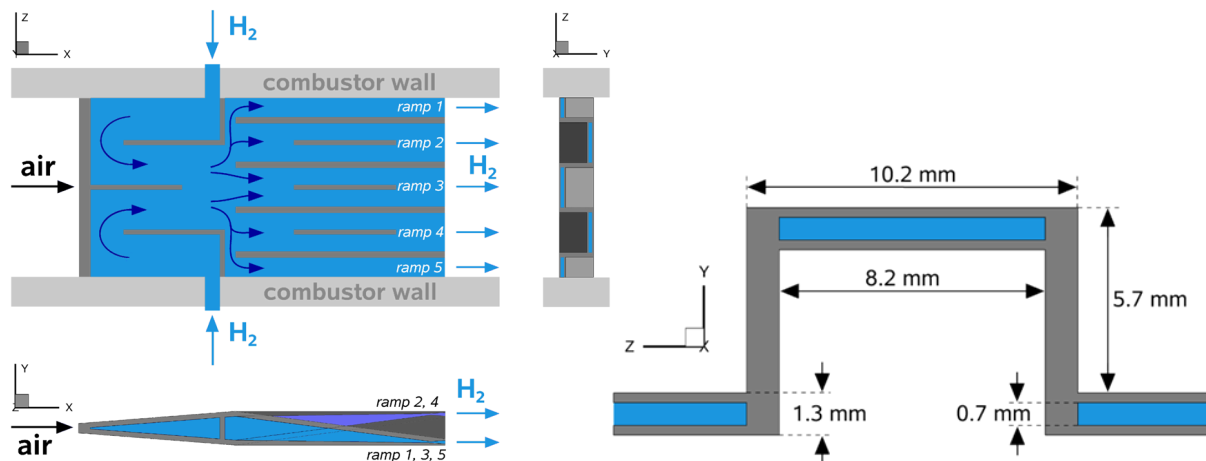

Fig 4. Interior structure of the strut and flow arrangement inside the strut (left side) with views from top, the side (below), and behind (right). Extension of the blunt end (right side) and sizes. Hydrogen is depicted in blue.

extreme temperatures. For this reason the investigated struts have a blunt front [6,7], which allows the internal coolant (hydrogen) to come close to the tip (see Fig. 3 left side). Disadvantage of the blunt front is an associated small detached normal shock wave which, however, passes over quickly into an oblique shock. As will be shown later, the blunt front copper strut at Mach 8 flight conditions (total temperature of 3250 K) and $\Phi = 0.72$ has a lower maximum temperature (approximately 820 K) than the sharp tip strut at 1300 K total temperature.

Hydrogen is fed to the strut through the side walls by two rectangular channels, as indicated by arrows in Fig. 4 (see also Fig. 5 where the computational grid for the internal flow is shown). All sizes of the lobed end are given on the right side. Figure 4 additionally shows the hydrogen flow inside the strut. Hydrogen is first directed towards the tip in order to achieve a good cooling of the thermally highly loaded front part. At the tip the flow direction is changed and on its way to the nozzle the hydrogen flux is split over the different ramps before injection. Nozzles inside the strut accelerate the hydrogen up to a Mach number of approximately 2.3 at the nozzle exit. The thicknesses of the internal walls needed to force the hydrogen flow in the desired directions is 1 mm. This corresponds to the thicknesses of the upper and lower walls. Due to the limited depth of the strut (18.4 mm from the side wall to the middle axis), the side walls, which are assumed to have a constant temperature, contribute to cooling the strut. However, the greatest part of the heat taken by the strut is transferred to the hydrogen and thus is
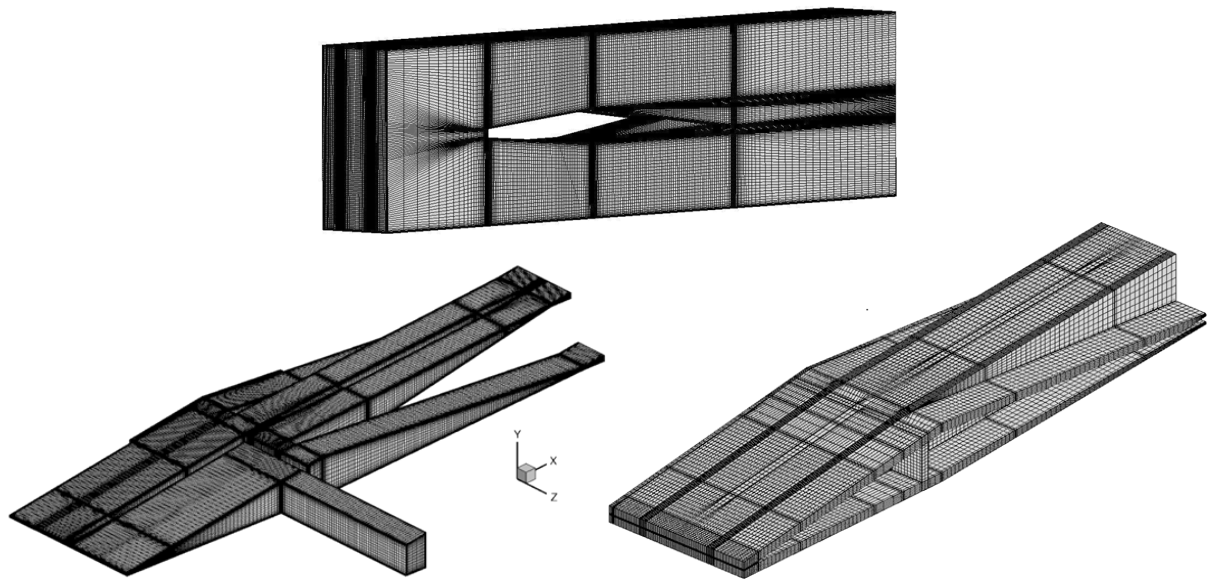
Fig 5. Computational grids for the external channel flow (upper figure), the strut internal flow (lower figure left side), and for the heat conduction simulation in the strut material (lower figure right side).

used regeneratively. Moreover, the heated hydrogen reduces the ignition delay time and therefore, at critical conditions, contributes to flame stabilization.

3.2. Computational grid, numerical set-up, and coupling

Due to the complex geometrical structure of the strut injector its computational grid requires a large number of blocks for discretization. Besides the lobed structure at the end of the strut, a number of internal walls are needed to first direct the hydrogen towards the tip and later to separate it uniformly over the different ramps. The corresponding grids for the internal fluid flow and the strut material are plotted (left and right) in the lower figures of Fig. 5. The grid of the external channel flow is shown on top. In order to reduce the computational cost, only one half of the channel/strut is simulated, what is sufficient for steady-state RANS simulations. Symmetry boundary conditions are assumed at the channel middle plane. Due to the requirements of the q-ω low-Reynolds number turbulence model and to accurately resolve the heat fluxes at the walls, very fine grids ($y^+ \approx 1$) are used for all near wall regions. The mesh in the solid is also strongly refined at all solid/fluid interfaces. In total the grid consists out of 463 blocks and 6.86 million volumes. The grid for the strut is divided into 327 blocks and has 0.417 million volumes. The grid for the internal flow has 54 blocks and 1.568 million volumes, and the grid for the external flow consists out of 82 blocks and 4.878 million volumes. If required for parallelization these blocks are further divided according to the number of available CPUs.

All simulations presented in this paper use identical air inflow boundary conditions at the left side of the combustion chamber (see Fig. 2), which correspond to Mach 8 flight conditions. Due to the supersonic speed all inflow values are fixed. Hydrogen enters the strut through a fuel supply tube at subsonic speed. Here a mass flux boundary condition is employed to achieve a desired mass flux. The inflow conditions for air and hydrogen are summarized in Table 1. Depending on the chosen inlet pressure for hydrogen, three equivalence ratios (Φ = 0.18, 0.36, and 0.72) are realized. In all cases a constant wall temperature of T_w = 450 K is set at the combustion chamber walls as well as at the walls of the hydrogen supply tubes, which cross the side walls.

For the steady-state results presented later, the internal and external flow fields as well as the temperature field of the strut are calculated separately. After a specified number of iterations, boundary data (λ_g, T_g, Δy_g and T_w, see Sect. 2) is exchanged. Between 15 and 20 of such cycles are required to

Table 1. Inflow conditions for air (combustion chamber) and hydrogen (strut injector). The hydrogen inlet pressures result in equivalence ratios of Φ = 0.18, 0.36, and 0.72.

	Air	hydrogen
Mach number (-)	3.0	0.13
Static temperature (K)	1160	290
Total temperature (K)	3250	291
Velocity (m/s)	2003	290
Static pressure (bar)	0.97	12.0 / 24.0 / 48.0
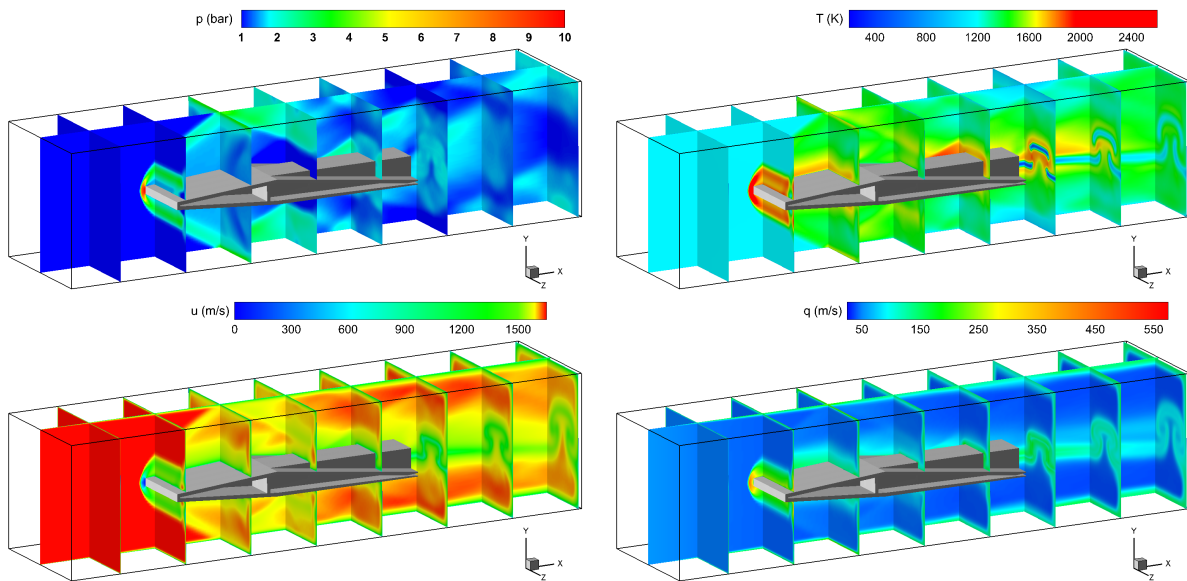
Fig 6. Channel flow fields around the standard SiC strut injector at Φ = 0.18. Upper figures: Pressure and temperature, lower figures: Axial velocity and turbulence variable q.

achieve a fully converged solution. However, this is only possible if an extrapolation of the exchanged data is performed [7]. Otherwise nearly twice as much couplings and iterations are needed. For every coupling cycle approximately 10,000 iterations are performed for the internal flow, 30,000 for the external flow, and 90,000 for the strut material, respectively. This is because of the strongly different temporal behaviors of the supersonic and subsonic flows on one side, and the heat conduction in the solid on the other side. Because heat conduction is the slowest process, couplings are performed until the change in maximum strut temperature is lower than 1 K per cycle.

4. Results and discussion

In order to get an overview of the external flow field, Fig. 6 shows pressure, temperature, axial velocity, and turbulence variable ($q = \sqrt{k}$) contour plots for the simulated channel segment. The corresponding Mach number distribution is given on the left side of Fig. 7. The figures are for the standard strut geometry (see Fig. 3), an equivalence ratio of Φ = 0.18, and SiC (silicone carbide) as strut material. However, the external flow fields using different hydrogen mass fluxes, materials, and front thicknesses mainly differ close to the wall and thus, the given figures are representative for all simulations. All figures clearly show the shock wave in front of the strut which is reflected at the upper and lower channel walls and hits the strut again approximately after half of the lobed strut structure. As will be shown later the reflected shocks cause an increase in strut temperature and, beside the high temperature
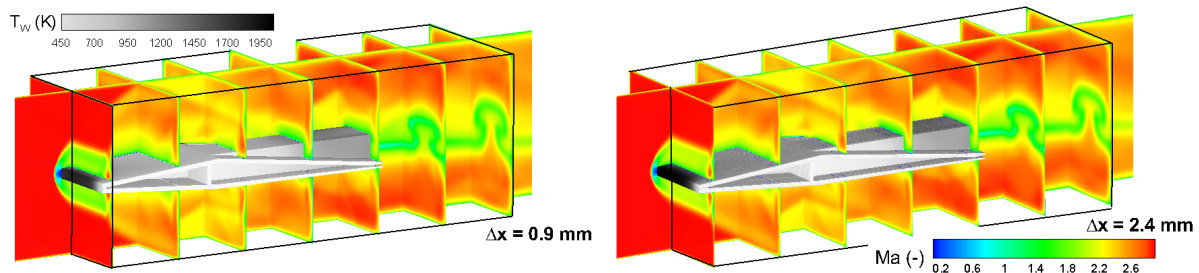
Fig 7. Mach number contours (in colour) and strut surface temperatures (black/white) of channel flow fields around SiC struts at $\Phi = 0.18$ with $\Delta x = 0.9$ mm (left side) and $\Delta x = 2.4$ mm (right side) front wall thickness.
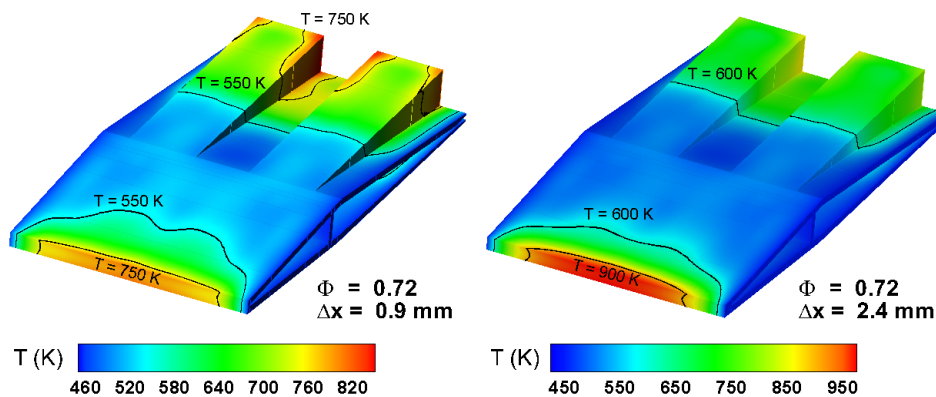

Fig 8. Simulated surface temperatures of lobed strut injectors with 0.9 mm (left side) and 2.4 mm (right side) front wall thickness (copper strut at $\Phi = 0.72$).

region at the tip, create a second region where peak temperatures may occur. The bow shock is also responsible for a small subsonic zone upstream of the blunt front with pressures up to 10 bar and strong turbulence production (see q contour plot). As a result, the flow field around the strut is completely turbulent. Downstream of the strut the lobed structure of the injected hydrogen becomes visible in the temperature, velocity, and q contour plots.

4.1. Influence of the front wall thickness of the strut

As described in Sect. 3.1, a sharp tip of the strut is difficult to cool and thus induces peak temperatures which are too high for most materials. As a consequence blunt fronts with thicknesses of $\Delta x = 2.4$ mm and 0.9 mm are investigated, as shown on the left side of Fig. 3. Mach number distributions for both geometries are given in Fig. 7. The impact of Δx on the front shock and the external flow field is minor and hardly visible. However, the strut temperatures significantly differ (strut temperatures are plotted in black/white in Fig. 7). This is shown more clearly in a second example in Fig. 8. The strut on the left side has 0.9 mm front wall thickness, the right one 2.4 mm. The legends are different and related to the individual peak temperatures. Results for copper struts at an equivalence ratio of 0.72 are given. However, the changes due to the described variation of Δx are similar for all investigated strut materials and hydrogen mass flow rates (see also Fig. 12). In the present case the maximum temperature is 1004 K for the $\Delta x = 2.4$ mm strut, while 859 K are reached with 0.9 mm front wall thickness. This is a reduction of 145 K in peak temperature. For lower hydrogen mass flow rates ($\Phi = 0.36$ and 0.18) the drops for copper struts are 140 K and 179 K, respectively. In case of the SiC struts from Fig. 7, the reduced front wall thickness causes a drop of 204 K in peak temperature (from 2050 K to 1846 K), as can bee seen from Fig. 12. Finally, Fig. 9 shows cuts at $z = 1$ mm (1 mm away from the middle plane)
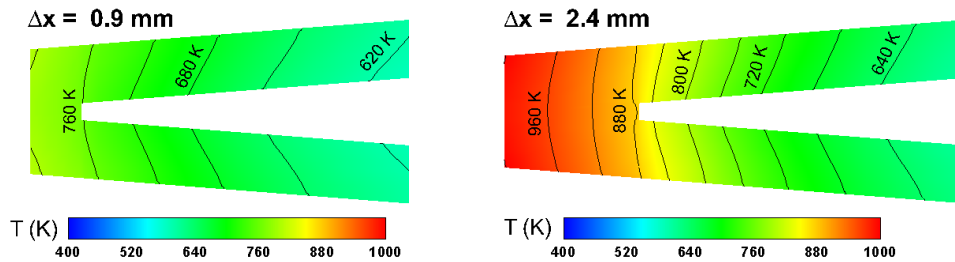
Fig 9. Simulated strut temperatures at the tips of struts with 0.9 mm (left side) and 2.4 mm (right side) front wall thickness (copper strut at $\Phi = 0.72$, $\Delta T = 40$ K, location of the cut is at $z = 1$ mm).

through the tips of the struts from Fig. 8. From these figures it becomes obvious, that the increased wall thickness at the front is responsible for the higher peak temperature. Because of the low height of the cooling channel at the front end (0.3 mm), the tip of the strut is not cooled optimally. This is evident in case of the $\Delta x = 2.4$ mm strut, but even the front of the $\Delta x = 0.9$ mm strut could be cooled better. Nevertheless, the smaller front wall thickness clearly outperforms the thicker one and the $\Delta x = 0.9$ mm configuration is defined to be the standard strut in the following investigations.

Beside the tip of the strut a second region, where high material temperature may occur, is in the rear part of the lobed structure. Here the reflected shocks from the upper and lower channel walls hit the strut and causes a temperature increase, as can be seen in Fig. 8. Especially the vertical walls of the lobed structure (which are not internally cooled as the horizontal ones) show high temperatures towards the end. In the investigated cases this is no serious problem because at low equivalence ratios, where the highest strut temperatures occur, the peak values are in the front part. Otherwise struts as in [9,12,18] could be used, where in contrast to the present ones hydrogen is injected through the vertical parts, too. Moreover, the cooling effect from the side walls is clearly visible in Fig. 8. This is the reason why the highest temperatures in the vertical walls are reached at those close to the channel axis.

4.2. Influence of the equivalence ratio

An important parameter for strut cooling and combustion is the mass flux of the hydrogen injected through the strut. Moreover, the mass flux of coolant should never fall below the required minimum value (for a given flight Mach number and strut). The investigated combustion chamber is equipped with a single strut injector. However, in real configurations it would be advantageous to use most of the incoming oxygen for combustion and burn close to stoichiometric conditions. While centrally located strut injectors are well suited to use the oxygen from the core flow, wall injectors would be able to additionally burn fuel with the oxygen, which still is available in the near wall regions. For these reasons equivalence ratios below one (0.18, 0.36, and 0.72) are used in the present strut injector study. The different equivalence ratios are realized by varying the inlet pressure at the fuel supply tubes while keeping inflow temperature and velocity constant (see Table 1). In this way the hydrogen mass flow rate is changed while the air main flow is kept constant.

Figure 10 shows hydrogen temperature (left side) and turbulence variable (right side) distributions inside the standard copper strut for three different equivalence ratios. The shown surfaces are always the middle planes located between the upper and lower walls. In the first half of the strut this plane is at $y = 0$ mm, while due to the ramps the plane is at $y \neq 0$ in the second half. Additionally, streamlines of the velocity fields are plotted. From picture to picture (top to bottom) the hydrogen mass flux is always doubled. This causes a reduction in hydrogen temperature. In case of the lowest equivalence ratio ($\Phi = 0.18$) the highest hydrogen temperatures of ≈ 800 K appear in the small recirculation zone at the front close to the middle axis (at $x \approx 2$ mm, $z \approx 2$ mm), and downstream of the short internal walls in the middle of every ramp (at $x \approx 75$ mm, $z \approx 0.5$ mm and 9 mm). These small high temperature areas disappear with increasing fuel mass flux. The short strut internal walls are used for flow homogenization. As can bee seen from the streamlines plotted in Fig. 10, there are vortices upstream of these walls
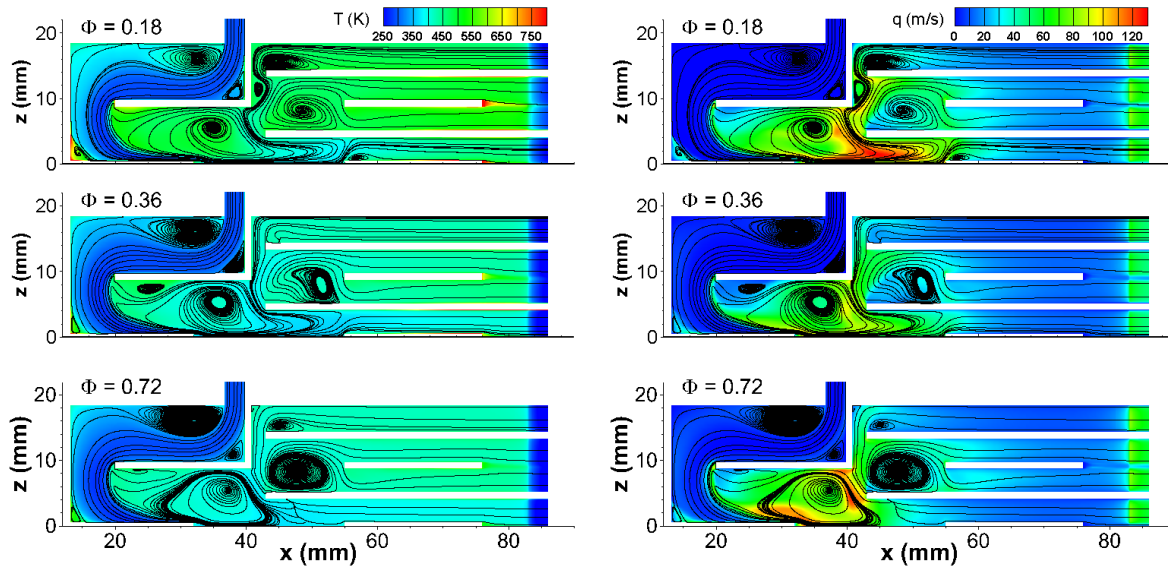
Fig 10. Temperature (left side) and turbulence variable q (right side) distributions in the middle plane between the upper and lower strut walls. The figures are for one half of the strut and different equivalence ratios ($\Phi = 0.18$, 36, and 72 from top to bottom). Additionally streamlines of the velocity fields are shown.

but there is a homogeneous flow field in axial direction towards nozzle and outflow. Because the shown contour plots are in the middle between the upper and lower walls, the temperatures increase as these walls are approached. With increasing equivalence ratio some of the smaller recirculation zones disappear and the flow is dominated by fewer, larger, and more stable vortices. The $q = \sqrt{k}$ contour plots (right side of Fig. 10) show a strong turbulence production after the flow direction has been changed towards the exit. The acceleration of the hydrogen in the nozzle (at $x \approx 83$ mm) causes a second increase in turbulence intensity shortly before injection.

The impact of an increased hydrogen mass flux on the strut surface temperature is illustrated in Fig. 11. Given are surface temperatures for the standard copper strut at equivalence ratios of 0.18 (left side) and 0.72 (right side). The peak temperatures at the front and at the end of the strut are significantly reduced by a higher hydrogen mass flow rate (please note the different maximum values of both legends). This
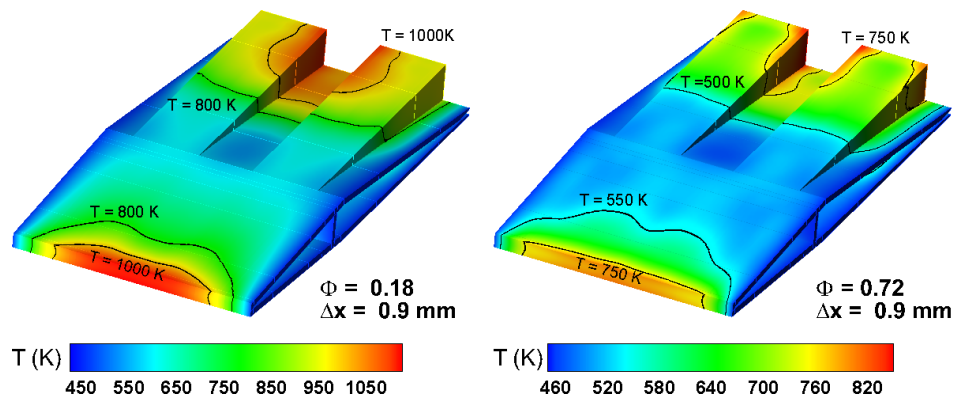

Fig 11. Simulated surface temperatures of the standard copper strut injector at equivalence ratios of $\Phi = 0.18$ (left side) and 0.72 (right side).
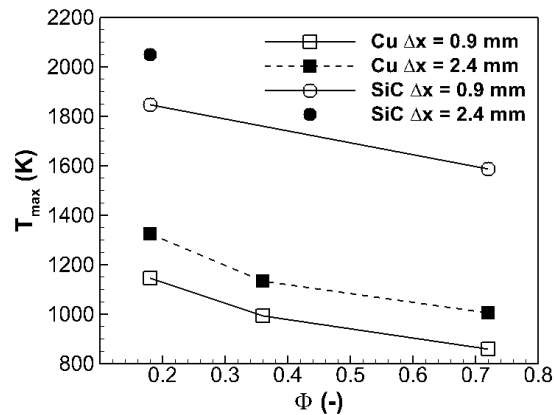
Fig 12. Strut material peak temperatures for copper and SiC struts, two front wall thicknesses, and varying equivalence ratios.

can also be observed in Fig. 12, where the maximum strut temperatures are plotted over the equivalence ratio for different front wall thicknesses and two strut materials. In all cases the peak temperatures significantly decrease with increasing hydrogen mass flux. For both, the standard copper and SiC strut the temperature reduction is $\approx$ 280 K if Φ is increased from 0.18 to 0.72. The increase in coolant mass flux also shifts the maximum temperatures from the front to the rear part of the strut. However, the differences between the front and rear maximum temperatures are relatively small. The largest heat load at the end of the strut is at the uncooled vertical walls of the lobed structure. This can be seen for the standard copper strut in Fig. 13, where a view from the back on the injection area of the strut is given. For a better comparison, identical legends are used for the Φ = 0.18 (left side) and 0.72 (right side) case. In the shown planes the peak temperatures are always in the middle of the vertical walls, closest to the symmetry plane (1116 K left side, 856 K right side). The injected hydrogen is significantly heated inside the strut. Its distribution over the exit area is quite non-uniform with strong temperature differences between the boundary layer and the middle of the injected jet. This can be clearly seen in the left plot of Fig. 13, where the hydrogen temperature reaches values of more than 1000 K directly at the wall, while it is quite cold ($\approx$ 285 K) in the middle. Moreover, the distributions of the injected hydrogen also differs from ramp to ramp [7].

Integrated heat fluxes (over the corresponding strut surfaces) from the external air flow towards the strut, from the strut to the internal hydrogen flow, and from the strut to the combustion chamber side walls are given in Fig. 14. Plotted are heat flux values for copper and SiC struts at different stoichiometric ratios and front wall thicknesses. With respect to the copper struts it can be observed, that the influence of the front wall thickness on the total heat fluxes is negligible. This is in contrast to
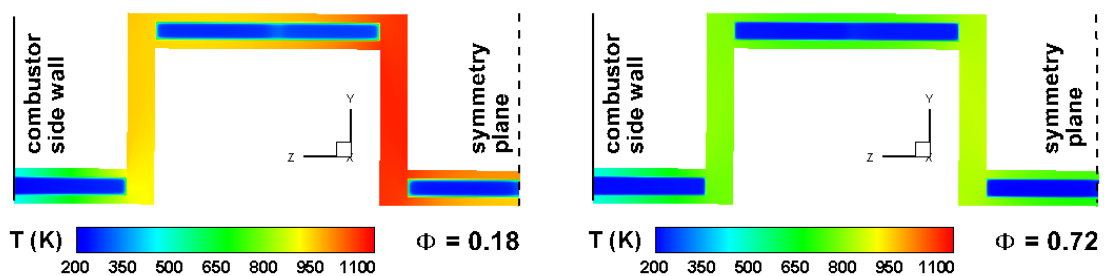

Fig 13. Surface temperature distribution of the strut material and temperature of the injected hydrogen at the strut end in a view from the back. Left side Φ = 0.18, right side Φ = 0.72, standard copper strut.
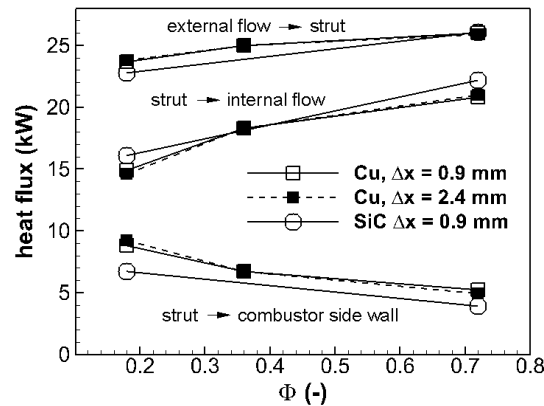
Fig 14. Integrated heat fluxes for copper and SiC struts with 0.9 mm (copper and SiC) and 2.4 mm (copper) front wall thickness at different equivalence ratios.

the peak temperature, where a smaller front wall thickness Δx can be crucial for the strut to survive. Figure 14 also shows a rise in the heat fluxes from the air to the strut and from the strut to hydrogen if Φ is increased, while at the same time the heat fluxes to the side walls decrease. A four times higher hydrogen mass flux increases the heat flux to the strut by 8.8% only, but the heat flux from the strut to the hydrogen by 39.6%. In case of the copper struts between 62.9% ($\Phi = 0.18$ and $\Delta x = 0.9$ mm) and 81.1% ($\Phi = 0.72$ and $\Delta x = 2.4$ mm) of the heat flux from the air to the strut is recovered by the injected hydrogen. The remaining heat is transferred to the combustor walls and may also be used regeneratively. The impact of different strut materials on the heat fluxes will be discussed in the next section. The averaged heat flux (25 kW) from the external flow to the strut corresponds to approximately 3.5 MW/m^2. This is somewhat higher than the specific heat fluxes obtained in the boundary layer flow of Fig. 1. Probable reasons are the detached normal shock wave at the front and the shorter length of the strut, compared to the 1 m wall length taken in Fig. 1.

4.3. Influence of the strut material properties

Finally different strut materials with varying heat conductivities, specific heats, and densities are investigated. This is not done with the intention to promote a certain strut material. in principle a large number of materials exists, a strut may be manufactured from. But there are many aspects which have to be considered to find a suitable material. This, however, is not the subject of this paper. Instead we investigate the impact of different strut material properties, which roughly correspond to those of copper, molybdenum, tungsten, and silicon carbide.

Figure 15 shows temperature dependencies of the thermal conductivities $\lambda(T)$ and thermal diffusivities $a(T) = \lambda(T)/(\rho c_p(T))$ of the materials mentioned before. The thermal diffusivity is a measure how fast heat diffuses in the given solid. While the data for copper is plotted up to 1250 K maximum temperature, the remaining properties are given up to 2000 K, which may be higher than the practical usability of the materials. The references for the material property data as well as the material densities are summarized in Table 2. From these data temperature dependent polynomials are formed and used in the simulations. Especially for SiC there is a large spectrum of varying grain sizes, porosities, and

Table 2. References for strut material data and densities used for the different materials.

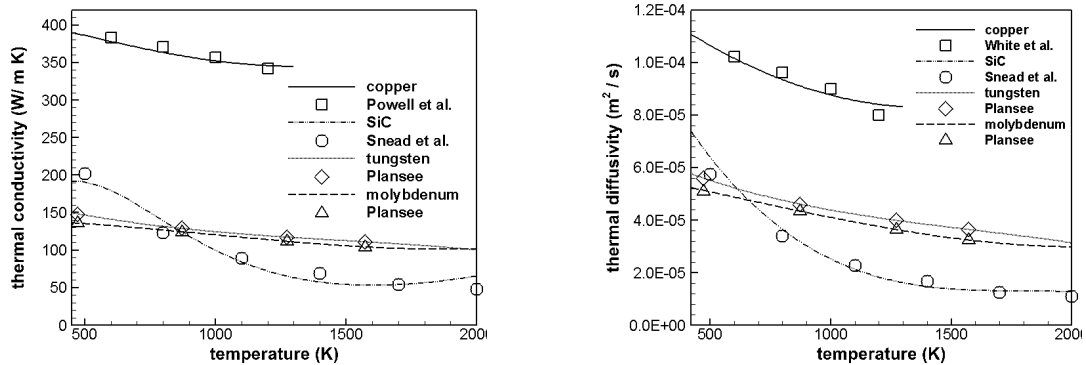|	copper	molybdenum	tungsten	SiC
Ref. for λ, c_p, ρ	[30], [31], [31]	all [32]	all [32]	all [33]
ρ (kg/m^3)	$8.92 \cdot 10^3$	$10.2 \cdot 10^3$	$19.3 \cdot 10^3$	$3.21 \cdot 10^3$

Fig 15. Thermal conductivities (left side) and thermal diffusivities (right side) for different materials. Symbols - data from references, lines - polynomials used in the simulation.
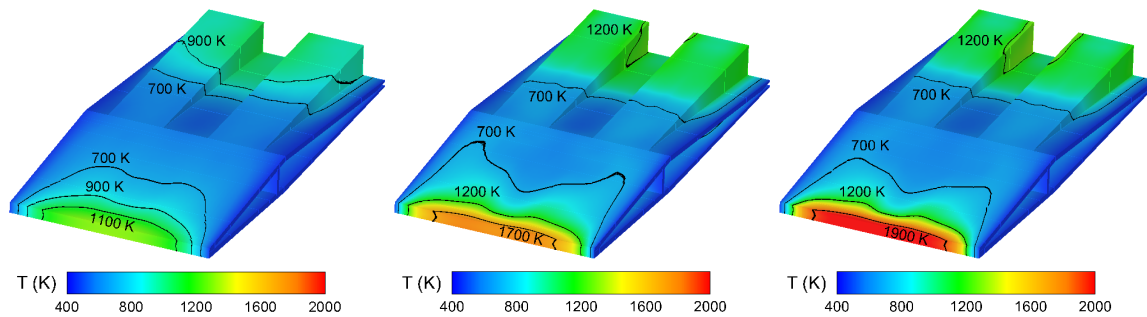

Fig 16. Calculated strut surface temperatures using different materials: Copper, molybdenum, and SiC from left to right.

combinations with fiber materials. Accordingly, the heat conductivities strongly differ. The chosen λ_{SiC} values of this paper probably are at the upper end. Molybdenum and tungsten have very similar heat conductivities and diffusivities despite their different densities. All materials have in common, that their heat diffusion reduces with increasing temperature.

The different strut materials are investigated for the worst conditions used in this paper which are an equivalence ratio of 0.18 and 2.4 mm front wall thickness. Figure 16 shows surface temperatures for copper, molybdenum, and SiC struts (from left to right). Because the differences between tungsten and molybdenum are minor, only the latter one is shown here. Identical legends are used for a better comparison. As expected, the peak temperatures increase from left to right due to the decreasing thermal diffusivity. The corresponding values are summarized in the first line of Table 3. Differences due to material properties mainly occur at the tip of the strut and, somewhat smaller, in the rear part. The peak temperatures of the copper and SiC struts differ by 725 K. Even in case of the better cooled

Table 3. Peak temperatures of the $\Delta x = 2.4$ mm strut at $\Phi = 0.18$ for different strut material (upper line) and heat fluxes from air to strut and strut to hydrogen (lower two lines) for the same strut and operating conditions.

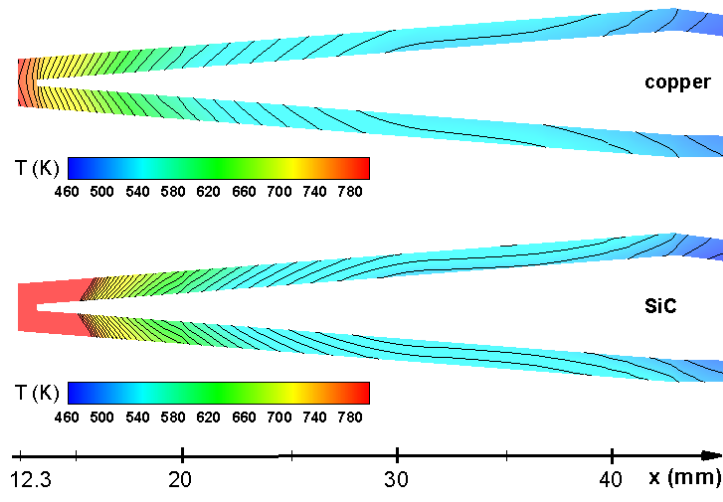|	copper	molybdenum	tungsten	SiC
T_{max} (K)	1325.3	1814.7	1795.1	2050.0
$q_{air-strut}$ (kW)	23.8	22.5	22.6	22.5
$q_{strut-H_2}$ (kW)	14.6	15.9	15.9	15.6

Fig 17. Cuts at $z = 2$ mm through the front parts of the standard copper (top) and SiC (bottom) struts for $\Phi = 0.72$ (isolines are plotted with $\Delta T = 10$ K).

strut with 0.9 mm front wall thickness, this difference is still 700 K, as can be seen from Fig. 12. One aim for practical applications should be to achieve a strut temperature distribution as homogeneous as possible. In the middle part of the struts (see Fig. 16), where the wall thickness is nearly uniform and all walls are cooled well, the disparity due to the different materials becomes very small (in the region between the 700 K isolines).

Figure 17 shows cuts through the front parts of the standard copper (upper figure) and SiC (lower figure) struts for $\Phi = 0.72$ which confirm the above given observations. The cuts are taken 2 mm away from the middle axis (at $z = 2$ mm) in order to avoid the vertical wall at the axis. Identical legends are used. Note, however, that the legend for the SiC strut and the isolines end at 800 K. While there are significant differences at the tip, the temperature distributions at $x > 17$ mm become quite similar. This can be seen on the left side of Fig. 18, too, where the outer and inner surface temperatures along the upper wall (at the interfaces from the solid to the outer air and to the inner hydrogen flow) are plotted for the cuts shown before. Between $x = 25$ mm and $x = 45$ mm the temperature profiles for copper and SiC at the strut/hydrogen interface are nearly identical. However, the temperatures at the air interfaces differ due to the different diffusivities of the materials. To show this more clearly, the corresponding temperature differences ΔT_W over the wall thickness are plotted for the upper wall on
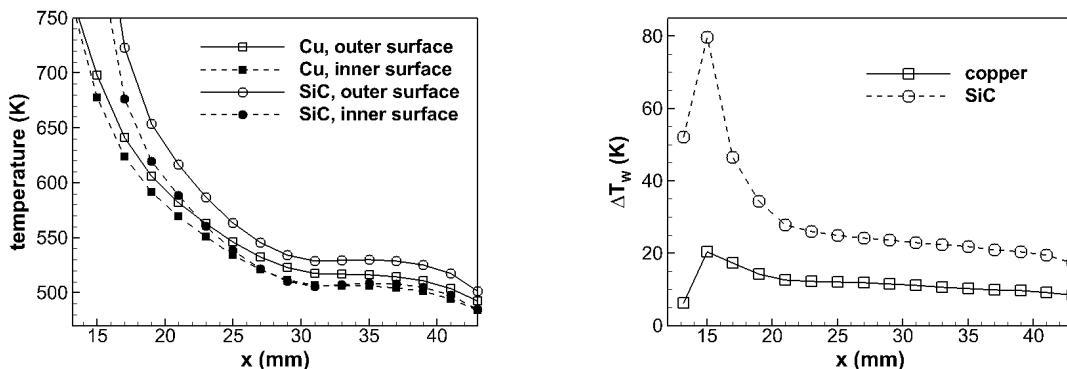

Fig 18. Temperature profiles (left side) along the outer and inner strut surface of the upper wall (see Fig. 17) and corresponding temperature differences (right side) for copper and SiC struts.

the right side of Fig. 18. For $x > 20$ mm, where the temperatures are below 600 K, ΔT_W for the SiC strut is approximately two times higher than that of the copper strut. This corresponds pretty well to the ratio of the thermal diffusivities at this temperature, as can be seen from Fig. 15. However, such a small change in ΔT_W hardly has any impact on the air or hydrogen temperature distributions.

Thus it can be summarized, that the different strut materials cause strongly varying peak temperatures at the front. Due to the uncooled vertical walls of the lobed structure there is a second high temperature region at the end, which again is influenced by material properties. In between is a large part of the strut, where the surface temperatures are hardly influenced by the material. Here the higher thermal diffusivity of copper causes a smaller ΔT_W over the wall thickness which, however, has a negligible impact on the heat transfer through the wall. The resulting integrated heat fluxes from the external flow to the strut as well as from the strut to the hydrogen are quite similar for the different materials, as shown in Fig. 14. In line two and three of Table 3 the integrated wall heat fluxes are given for the $\Delta x = 2.4$ mm strut at $\Phi = 0.72$ for all investigated materials. Again, the differences in wall heat flux stemming from material properties are smaller than 10%.

The presented results show, that the impact of thermal diffusivity in the first place becomes strong at locations, which are not efficiently cooled. On the other hand the heat flux to the coolant is strongly dominated by the surface temperature of the strut, as demonstrated in Fig. 1. Because the available cooling capacity is a critical factor, the effect of a reduced heat flux at higher temperatures could be used, if the strut material is able to withstand it. In this case the coolant would be used first to cool the combustor walls before it is fed to the strut. Due to the elevated temperature, the heat fluxes towards the strut would be significantly reduced. In this case local hot spots have to be avoided and the strut temperature should be as uniform as possible. Because the strut is always the last combustor part to be cooled before fuel injection, it will automatically be exposed to the highest temperatures.

4.4. Summary and Conclusions

In the presented numerical study small modifications of the front part of a lobed strut injector have been investigated. Moreover, different fuel mass fluxes and strut materials have been studied. All simulations are for Mach 8 flight conditions. It could be shown, that the standard copper strut is sufficiently cooled by the chosen internal hydrogen flow arrangement to work well at continuous operation. Important results of the study are

- a sharp tip of the strut can not be cooled and a small blunt front should be used;

- it is important to keep the strut temperature as homogeneous as possible;

- therefore, the strut material thickness should be as homogeneous as possible, too. In case of the present strut its length still could be reduced in order to increase the height of the internal hydrogen channel at the front. In this way the front part cooling should improve further;

- if the front part is cooled well, peak temperatures appear in the rear of the strut. This can be avoided if the vertical walls of the structure are cooled internally by hydrogen, too;

- the increase in strut peak temperature with decreasing equivalence ratio is relatively independent of the material. The lower limit for Φ depends on the maximum temperature the strut can withstand;

- in dependence on the strut and equivalence ratio, between 62% and 85% of the heat from the external flow is directly recovered by the hydrogen, the rest goes to the side walls;

- because the strut is the last object of a number of parts which have to be cooled, a strut material which is able to withstand high temperatures would be extremely useful because of the limited availability of coolant.

In comparison to many other strut injector concepts, the present one not only achieves a very good mixing (as shown before in [12, 18, 19]), but it also can be cooled efficiently, as demonstrated in this

paper. This is because external and internal flows are separated by walls of a relatively homogenous thickness and strong detached shocks are avoided.

Acknowledgement

References

1. Kanda, T., Masuya, G., Ono, F., Wakamatsu, Y.: Effect of Film Cooling/Regenerative Cooling on Scramjet Engine Performance. J. Prop. Pow. 10, 613-624 (1994)

2. Qin, J., Zhou, W., Bao, W., Yu, D.: Thermodynamic Optimization for a Scramjet Re-cooled Cycle. Acta Astronaut. 66, 1449-1457 (2010)

3. Song, K. D., Choi, S. H., Scotti, S.: Transpiration Cooling Experiment for Scramjet Engine Combustion Chamber by High Heat Fluxes. J. Prop. Pow. 22, 96-102 (2006)

4. Langener, T., von Wolfersdorf, J., Steelant, J.: Experimental Investigation on Transpiration Cooling for Scramjet Application Using Different Coolants. AIAA J. 49, 1409-1419 (2011)

5. Huang, H., Sobel, D. R., Spadaccini, L. j.: Endothermic Heat-Sink of Hydrocarbon Fuels for Scramjet Cooling. AIAA paper 2002-3871 (2002)

6. Gerlinger P., Simsont Y.-H.: Numerical Simulation of the Internal and External Flow Fields and Heat Fluxes of a Lobed Strut Injector. ISABE paper 2013-1627 (2013)

7. Simsont Y.-H., Gerlinger P.: High Order Numerical Simulation of the Thermal Load on a Lobed Strut Injector for Scramjet Application. Int. J. Numer. Meth. Fluids 82, 417-436, (2016)

8. Vergine V., Ground, C., Maddalena, L.: Strut Injectors for Scramjets: Total Pressure Losses in Two Streamwise Vortex Interactions. J. Prop. Pow. 33, 1140-1150 (2017)

9. Simsont Y.-H., Gerlinger P.: Numerical Investigation of a Complete Scramjet Model with Central Strut Injection. ISABE paper 2013-1619 (2013)

10. Dröske, N., Förster, F., Weigand, B., von Wolfersdorf J.: Thermal Investigation of an Internally Cooled Strut Injector for Scramjet Application at Moderate and Hot Gas Conditions. Acta Astronaut. 132, 177-191 (2017)

11. Srinivasan, K., Maurya, P. K., Abhishek, K., Desikan, S. L. N., Murugan B.: Supersonic Combustion of a Scramjet Engine Using Hydrogen Fuel in a Shock Tunnel. AIAA J. 56, 3600-3609 (2018)

12. Gerlinger P., Stoll P., Kindler M., Schneider F., Aigner M.: Numerical Investigation of Mixing and Combustion Enhancement in Supersonic Combustors by Strut Induced Streamwise Vorticity. Aerosp. Sci. Techn. 12, 159-168 (2008)

13. Gerlinger P., Nold, K., Aigner M.: Influence of Reaction Mechanisms, Grid Spacing, and Inflow Conditions on the Numerical Simulation of Lifted Supersonic Flames. Int. J. Numer. Meth. Fluids 62, 1357-1380, (2010)

14. Bouchez M.: Scramjet Thermal Management. Lecture von Karman Institute RTO-EN-AVT-185 (2010)

15. Scotti, S. J., Martin, C. J., Lucas, S. H.: Active Cooling Design for Scramjet Engines Using Optimization Methods. AIAA paper 88-2265 (1988)

16. Riggins, D., Tackett, R., Taylor, T., Auslender, A.: Thermodynamic Analysis of Dual-Mode Scramjet Engine Operation and Performance. AIAA paper 2006-8059 (2006)

17. Zhang, S., Qin, J., Xie, K., Feng, Y., Bao, W.: Thermal Behavior Inside Scramjet Cooling Channels at Different Channel Aspect Ratios. J. Prop. Pow. 32, 57-69 (2016)

18. Gerlinger P., Kasal, P., Stoll P., Brüggemann, D.: Experimental and Theoretical Investigation on 2D and 3D Parallel Hydrogen/Air Mixing in a Supersonic Flow. ISABE paper 2001-1019 (2001)

19. Kindler, M., Gerlinger P., Aigner, M.: Hybrid RANS/LES of Lobed Strut Injectors in Supersonic Flow. ISABE paper 2013-1625 (2013)

20. Gerlinger P., Stoll P., Brüggemann D.: An Implicit Multigrid Method for the Simulation of Chemically Reacting Flows. J. Comp. Phys. 146, 322-345 (1998)

21. Gerlinger P., Möbus, H., P., Brüggemann D.: An Implicit Multigrid Method for Turbulent Combustion. J. Comp. Phys. 167, 247-276 (2001)

22. Gerlinger P.: Multi-Dimensional Limiting for High-Order Schemes Including Turbulence and Combustion. J. Comp. Phys. 231, 2199-2228 (2012)

23. Jameson, A., Yoon, S.: Lower Upper Implicit Schemes with Multiple Grids for the Euler Equations. AIAA J. 25, 929-935 (1987)

24. Shuen S.J.: Upwind Differencing and LU Factorization for Chemical Non-Equilibrium Navier-Stokes Equations. J. Comp. Phys. 99, 233-250 (1992)

25. Coakley T.J., Huang P.G.: Turbulence Modeling for High Speed Flows. AIAA paper 92-0436 (1992)

26. Liou M.S.: A Sequel to AUSM – Part II: AUSM$^+$-up for all Speeds. J. Comp. Phys. 214, 137-170 (2006)

27. Choi, Y. H., Merkle, C. L.: The Application of Preconditioning in Viscous Flows. J. Comp. Phys. 105, 207-223 (1993)

28. Douglas J., Gunn J. E.: A General Formulation of Alternating Direction Methods – Part I: Parabolic and Hyperbolic Problems. J. Num. Math. 6, 428-453 (1964)

29. Anderson D. A., Tannehill J. C., Pletcher R. H.: Computational Fluid Mechanics and Heat Transfer (2nd). Hemisphere Publishing Corporation: New York Washington Philadelphia London, 1984

30. Powell R. W., Ho, C. Y., Liley, P. E.: Thermal Conductivity of Selected Materials. NSRDS-NBS 8, Washington, D.C. (1966)

31. White, G. K., Collocott S. J.: Heat Capacity of Rererence Materials: Cu and W. J. Phys. Chem. Ref. Data. 13, 1251-1287, (1984)

32. Werkstoffe. https://www.plansee.com/de/werkstoffe.html (2018), Accessed Oct. 2018

33. Snead, L. L., Nozawa, T., Katoh, Y., Byun, T.-S., Kondo, S., Petti, A. D.: Handbook of SiC Properties for Fuel Performance Modeling. J. Nuc. Mat. 371, 329-377 (2007)